Supporting Information for

Atomically Dispersed Dual-Metal Sites Showing Unique Reactivity and Dynamism for Electrocatalysis

Jun-Xi Wu[1,#], Wen-Xing Chen[3,#], Chun-Ting He[1,2,*], Kai Zheng[1], Lin-Ling Zhuo[1], Zhen-Hua Zhao[1], and Jie-Peng Zhang[1,*]

[1]MOE Key Laboratory of Bioinorganic and Synthetic Chemistry, School of Chemistry, Sun Yat-Sen University, Guangzhou 510275, P. R. China

[2]Key Lab of Fluorine and Silicon for Energy Materials and Chemistry of Ministry of Education, College of Chemistry and Chemical Engineering, Jiangxi Normal University, Nanchang 330022, P. R. China

[3]Energy & Catalysis Center, School of Materials Science and Engineering, Beijing Institute of Technology, Beijing 100081, P. R. China

[#]Jun-Xi Wu and Wen-Xing Chen contributed equally to this work.

*Corresponding author. E-mail: hct@jxnu.edu.cn (C.-T. He),

zhangjp7@mail.sysu.edu.cn (J.-P. Zhang)

S1 Text XAFS Data Processing

The acquired EXAFS data were extracted and processed according to the standard procedures using the ATHENA module implemented in the IFEFFIT software packages. The k^3-weighted EXAFS spectra were obtained by subtracting the post-edge background from the overall absorption and then normalized with respect to the edge-jump step. Subsequently, k^3-weighted $\chi(k)$ data of Co K-edge and Ni K-edge were Fourier transformed to real (R) space using a Hanning window (dk=1.0 Å^{-1}) to separate the EXAFS contributions from different coordination shells. To obtain the quantitative structural parameters around central atoms, least-squares curve parameter fitting was performed using the ARTEMIS module of IFEFFIT software packages [1].
The following EXAFS equation was used:

$$\chi(k)=\sum_j \frac{N_j S_o^2 F_j(k)}{k R_j^2}\exp[-2k^2\sigma_j^2]\exp[\frac{-2R_j}{\lambda(k)}]\sin[2kR_j+\phi_j(k)]$$

Where S_0^2 is the amplitude reduction factor, $F_j(k)$ is the effective curved-wave backscattering amplitude, N_j is the number of neighbors in the jth atomic shell, R_j is the distance between the X-ray absorbing central atom and the atoms in the jth atomic shell (backscatterer), λ is the mean free path in Å, $\phi_j(k)$ is the phase shift (including the phase shift for each shell and the total central atom phase shift), σ_j is the Debye-Waller parameter of the jth atomic shell (variation of distances around the average R_j). The functions $F_j(k)$, λ and $\phi_j(k)$ were calculated with the ab initio code FEFF8.2.

S2 Supplementary Figures and Tables

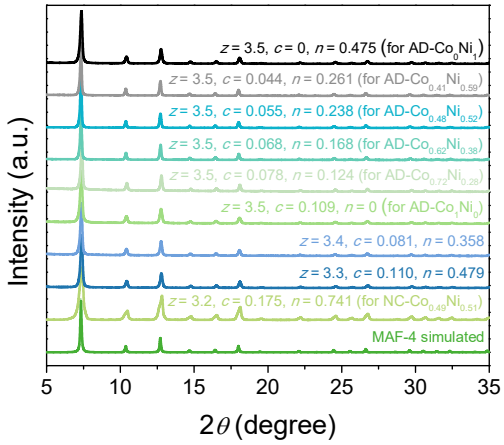

Fig. S1. PXRD patterns of Co/Ni-doped MAF-4.

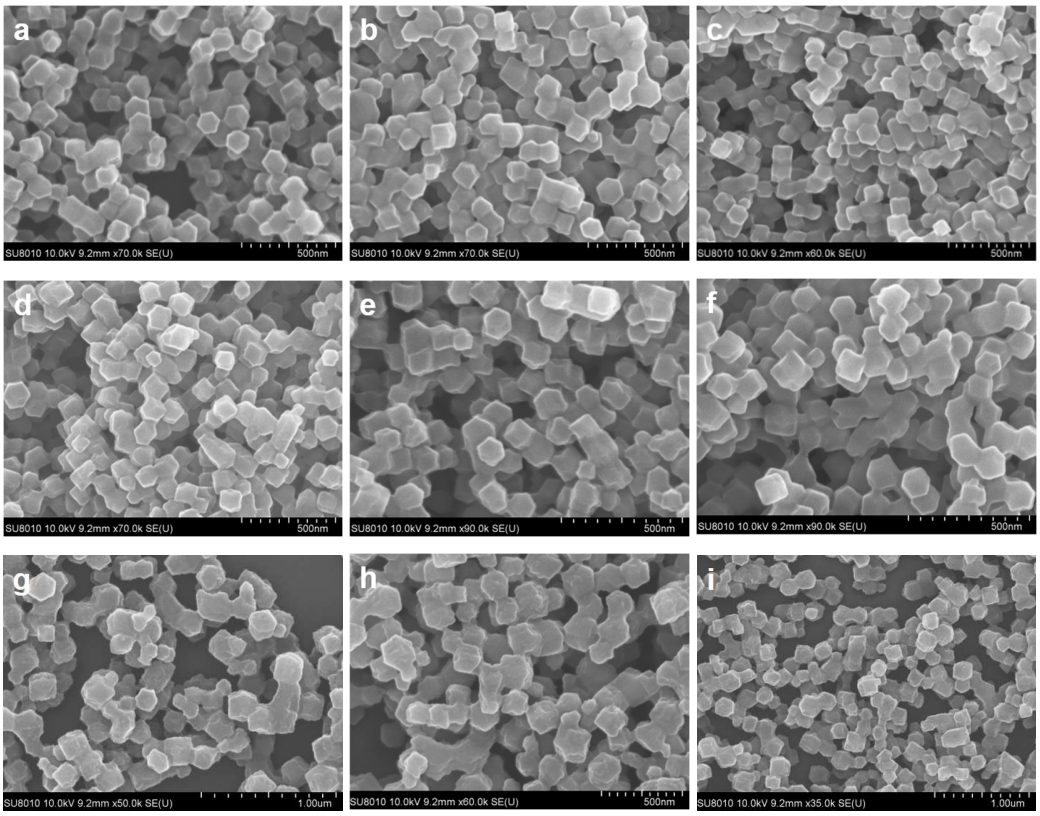

Fig. S2. SEM images of Co/Ni-doped MAF-4. (a) $z = 3.5$, $c = 0.109$, $n = 0$ (for AD-Co_1Ni_0), (b) $z = 3.5$, $c = 0.078$, $n = 0.124$ (for AD-$Co_{0.72}Ni_{0.28}$), (c) $z = 3.5$, $c = 0.068$, $n = 0.168$ (for AD-$Co_{0.62}Ni_{0.38}$), (d) $z = 3.5$, $c = 0.055$, $n = 0.238$ (for AD-$Co_{0.48}Ni_{0.52}$), (e) $z = 3.5$, $c = 0.044$, $n = 0.261$ (for AD-$Co_{0.41}Ni_{0.59}$), (f) $z = 3.5$, $c = 0$, $n = 0.475$ (for AD-Co_0Ni_1), (g) $z = 3.4$, $c = 0.081$, $n = 0.358$, (h) $z = 3.3$, $c = 0.110$, $n = 0.479$, (i) $z = 3.2$, $c = 0.175$, $n = 0.741$ (for NC-$Co_{0.49}Ni_{0.51}$).

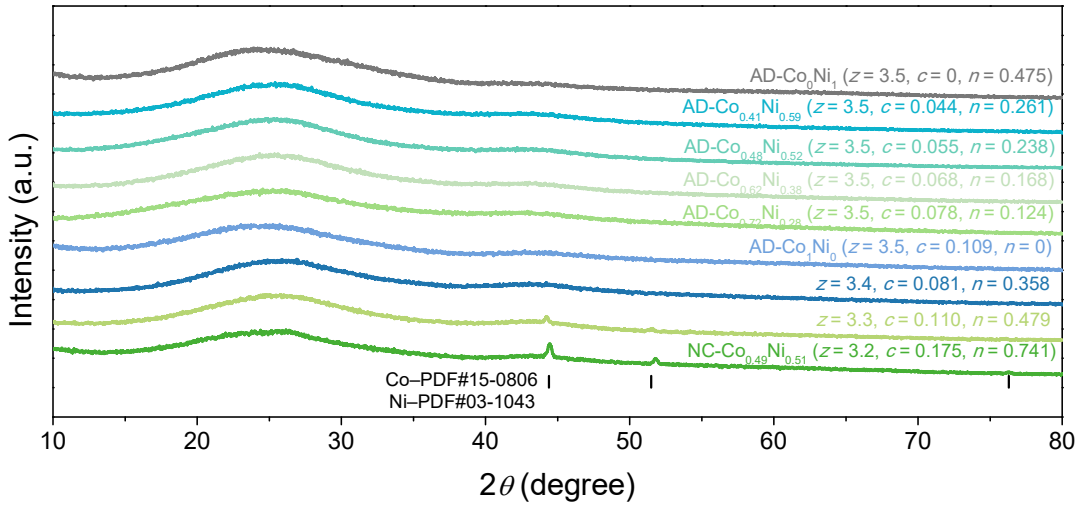

Fig. S3. PXRD patterns of the pyrolysis products of Co/Ni-doped MAF-4.

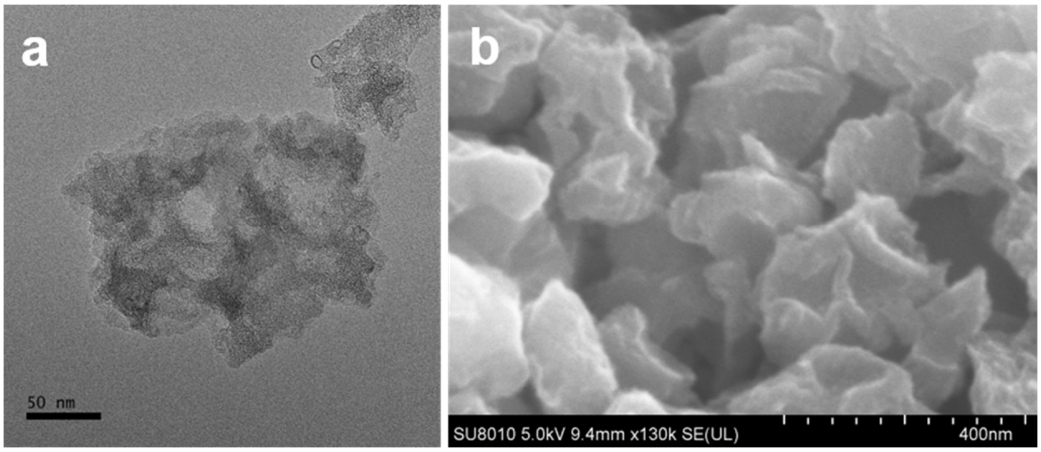

Fig. S4. (a) TEM and (b) SEM images of AD-Co_1Ni_0.

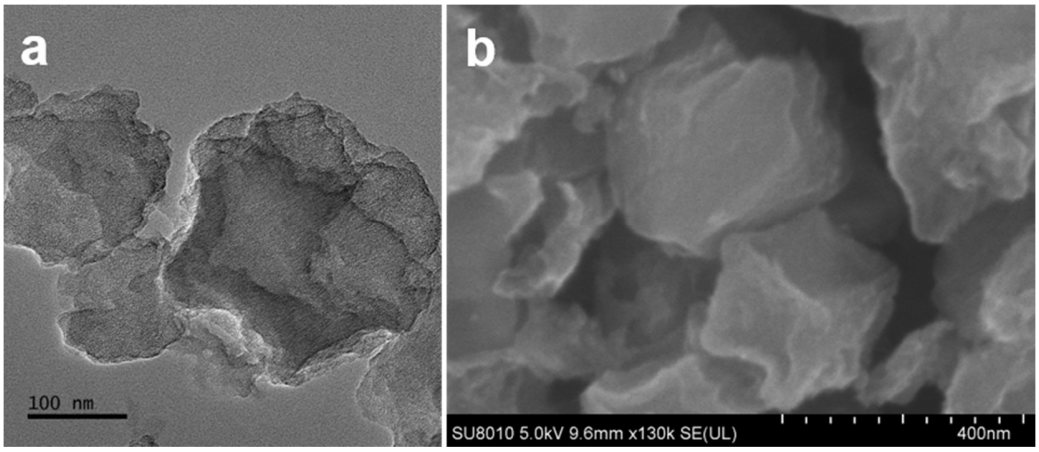

Fig. S5. (a) TEM and (b) SEM images of AD-$Co_{0.72}Ni_{0.28}$.

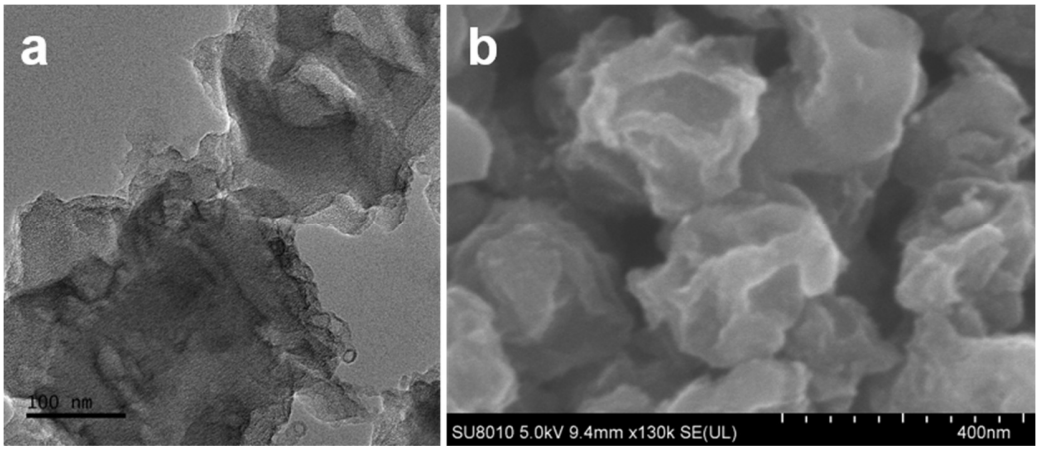

Fig. S6. (a) TEM and (b) SEM images of AD-$Co_{0.62}Ni_{0.38}$.

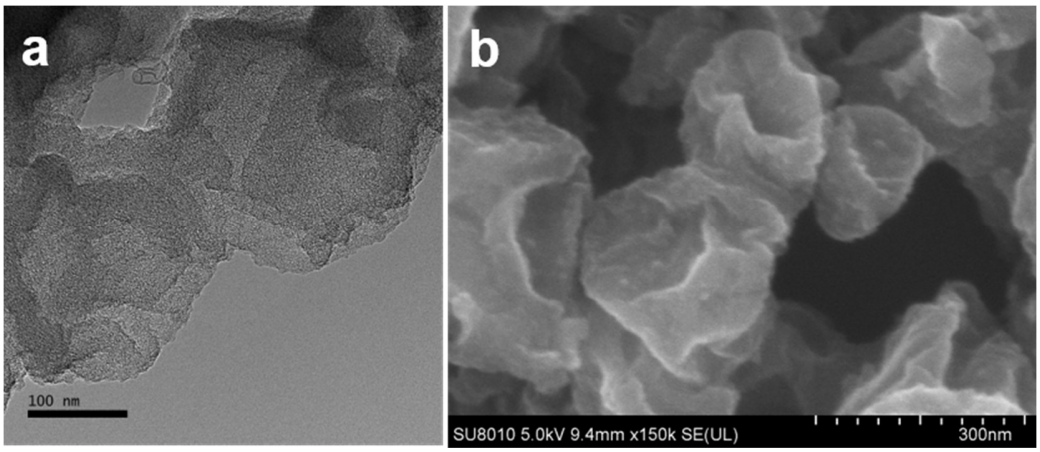

Fig. S7. (a) TEM and (b) SEM images of AD-$Co_{0.41}Ni_{0.59}$.

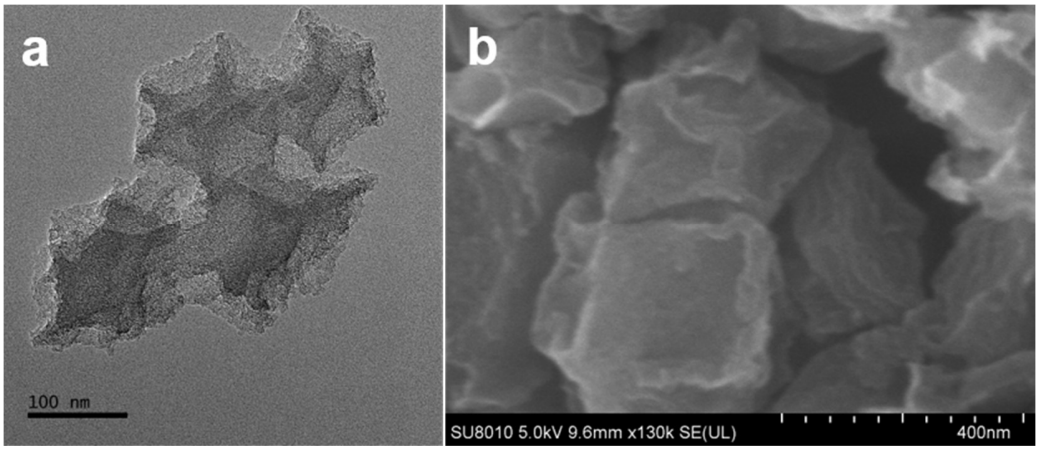

Fig. S8. (a) TEM and (b) SEM images of AD-Co_0Ni_1.

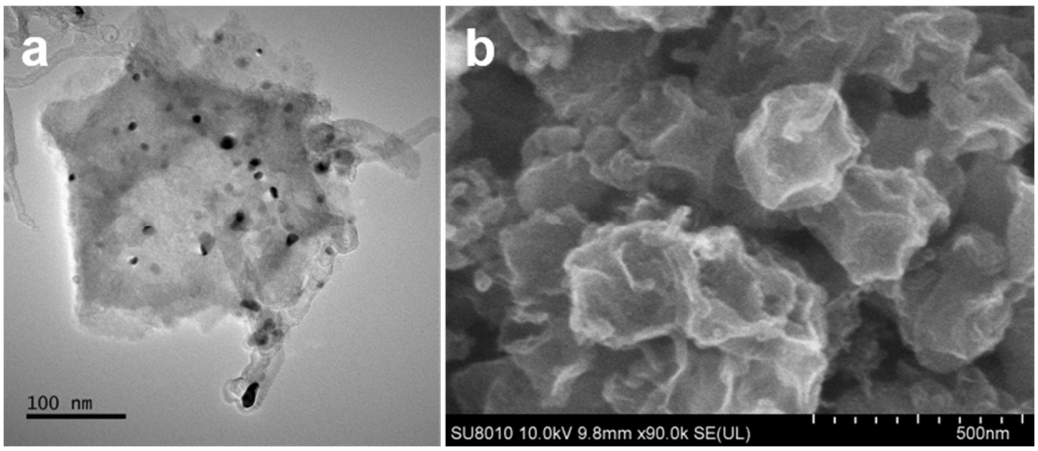

Fig. S9. (a) TEM and (b) SEM images of NC-$Co_{0.49}Ni_{0.51}$.

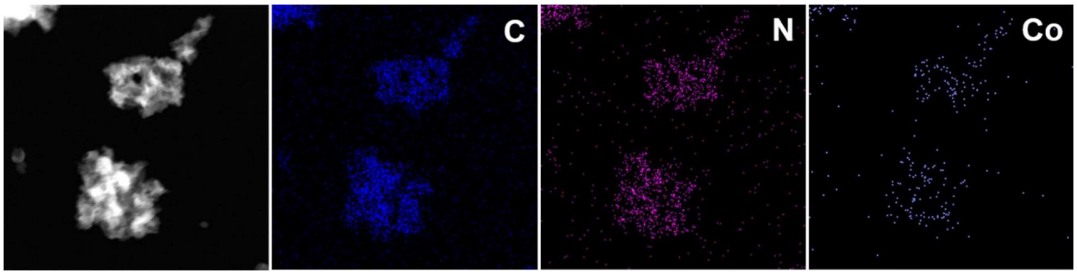

Fig. S10. HAADF-STEM and EDS of AD-Co_1Ni_0.

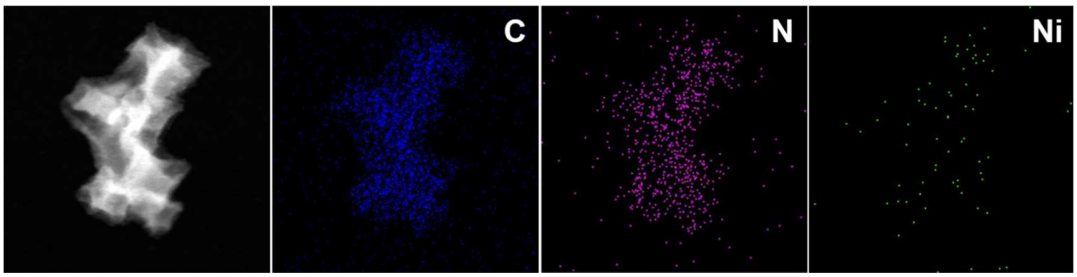

Fig. S11. HAADF-STEM and EDS of AD-Co_0Ni_1.

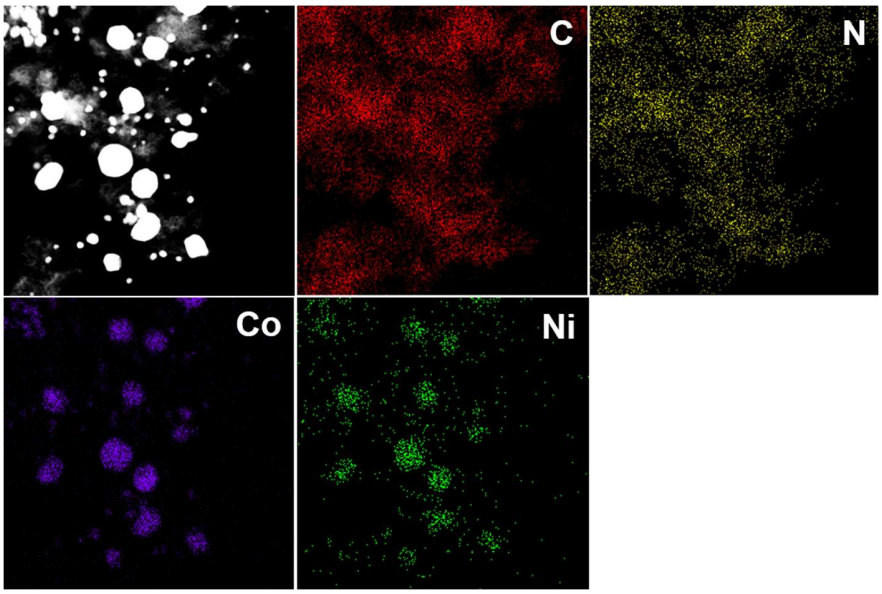

Fig. S12. HAADF-STEM and EDS of NC-$Co_{0.49}Ni_{0.51}$.

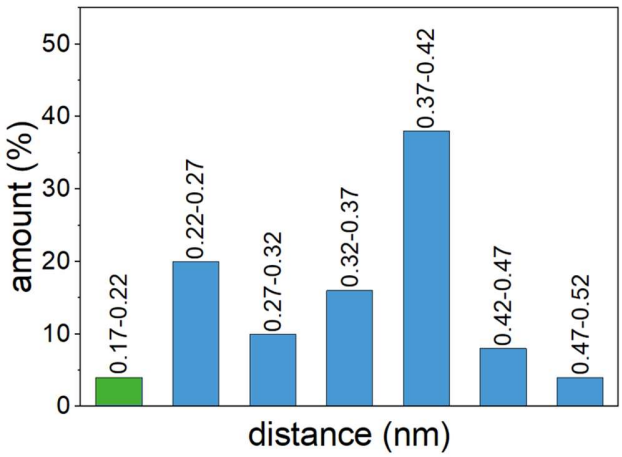

Fig. S13. Distribution of distances between adjacent bright dots in Fig. 1f. The distances less than 2.2 Å can be attributed to the overlap of metal atoms at different heights.

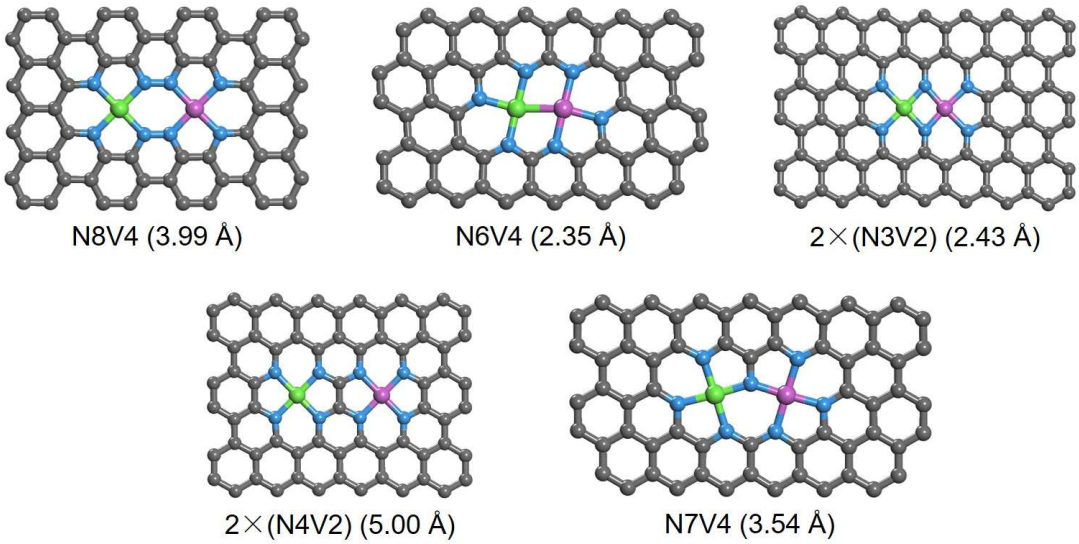

Fig. S14. The five different dual metal sites models denoted as N8V4 (3.99 Å), N6V4 (2.35 Å), 2×(N3V2) (2.43 Å), 2×(N4V2) (5.00 Å), and N7V4 (3.54 Å).

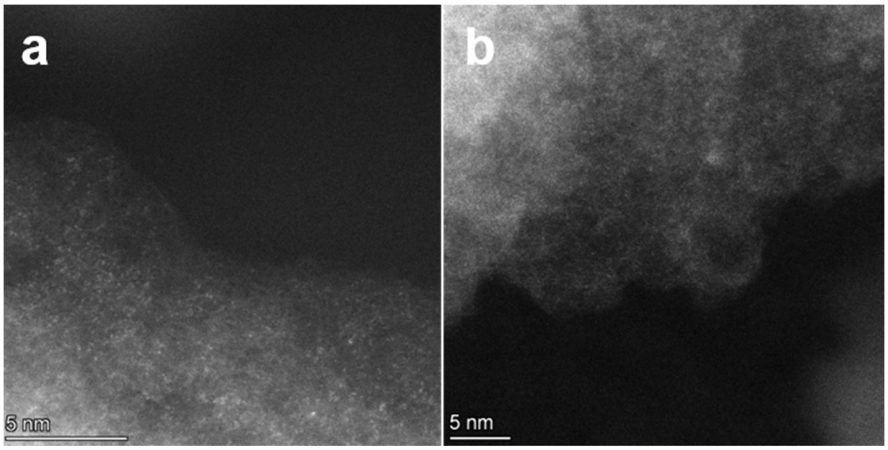

Fig. S15. HAADF-STEM images of (a) AD-Co_1Ni_0 and (b) AD-Co_0Ni_1.

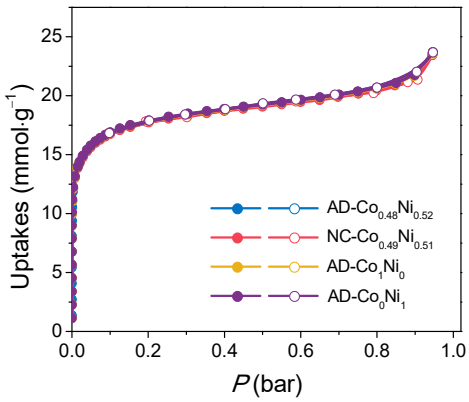

Fig. S16. 77 K N_2 adsorption isotherms of AD-Co_1Ni_0, AD-Co_0Ni_1, AD-$Co_{0.48}Ni_{0.52}$, NC-$Co_{0.49}Ni_{0.51}$.

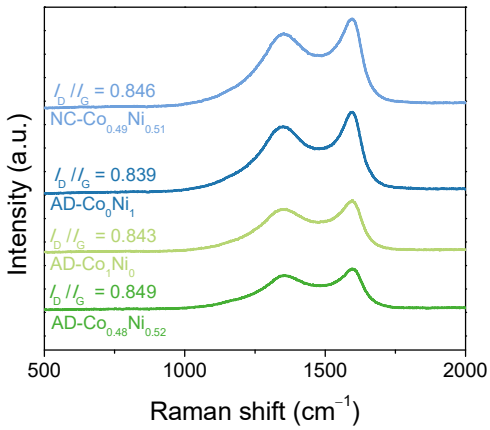

Fig. S17. Raman spectra of AD-$Co_{0.48}Ni_{0.52}$, AD-Co_1Ni_0, AD-Co_0Ni_1, and NC-$Co_{0.49}Ni_{0.51}$.

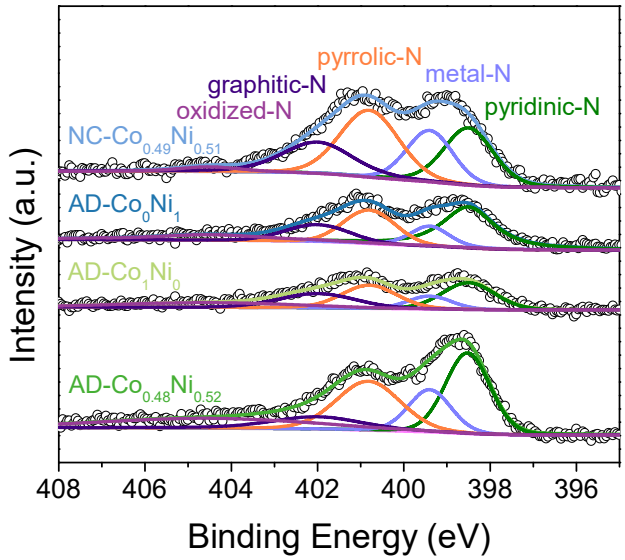

Fig. S18. High resolution XPS spectrum of AD-$Co_{0.48}Ni_{0.52}$, AD-Co_1Ni_0, AD-Co_0Ni_1, and NC-$Co_{0.49}Ni_{0.51}$ at the N 1s region.

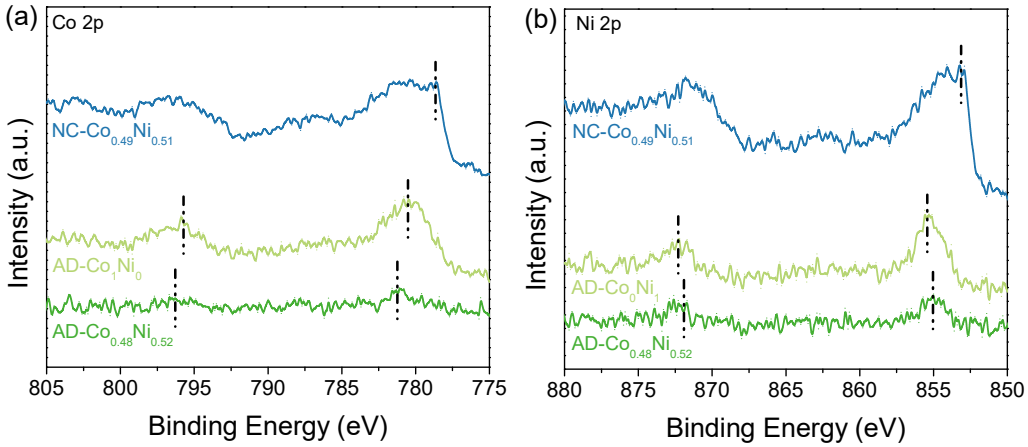

Fig. S19. High resolution XPS spectra of AD-$Co_{0.48}Ni_{0.52}$, AD-Co_1Ni_0, AD-Co_0Ni_1, and NC-$Co_{0.49}Ni_{0.51}$ at the (a) Co 2p and (b) Ni 2p region.

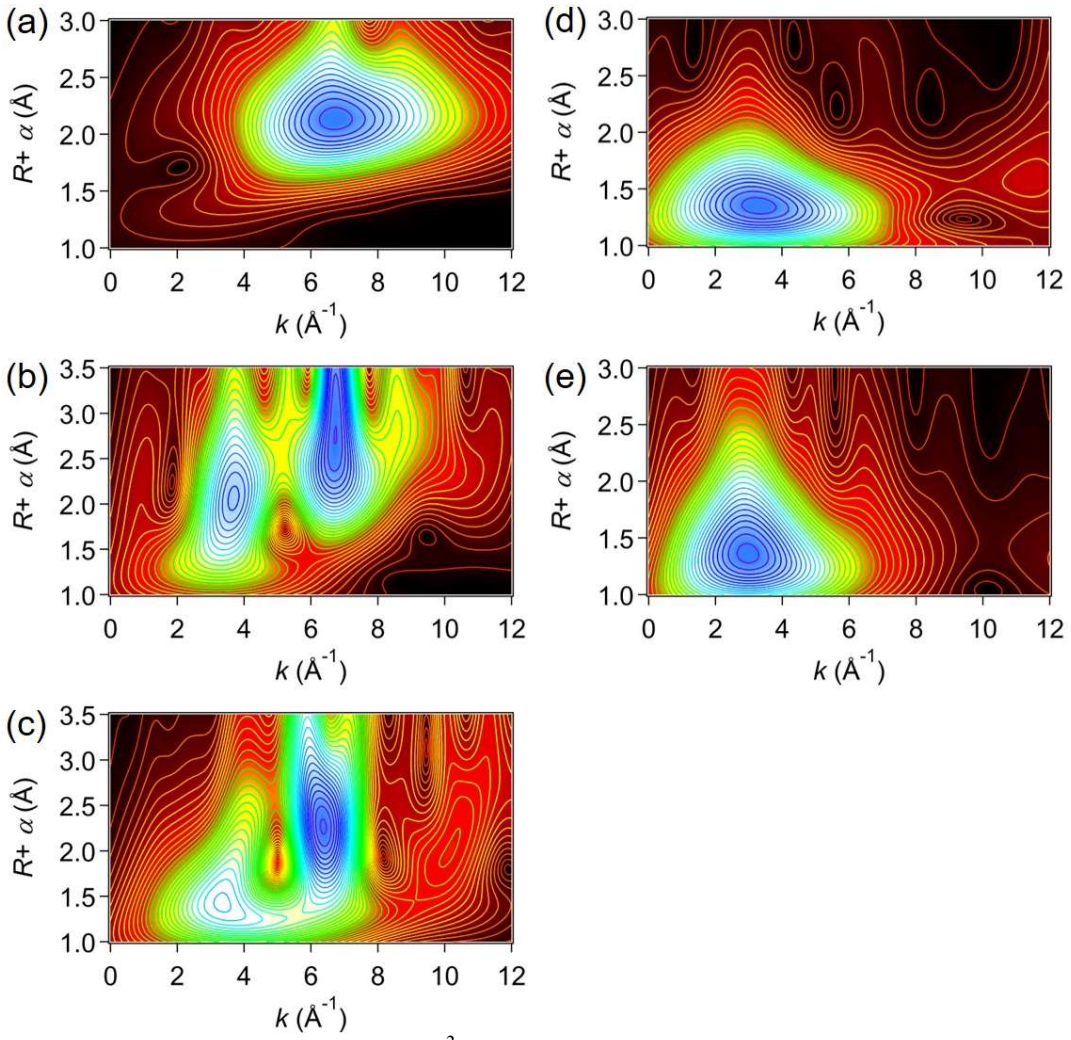

Fig. S20. Wavelet transforms for the k^3-weighted Co K-edge EXAFS signals of (a) Co foil, (b) CoO, (c) Co_3O_4, (d) AD-$Co_{0.48}Ni_{0.52}$, and (e) AD-Co_1Ni_0.

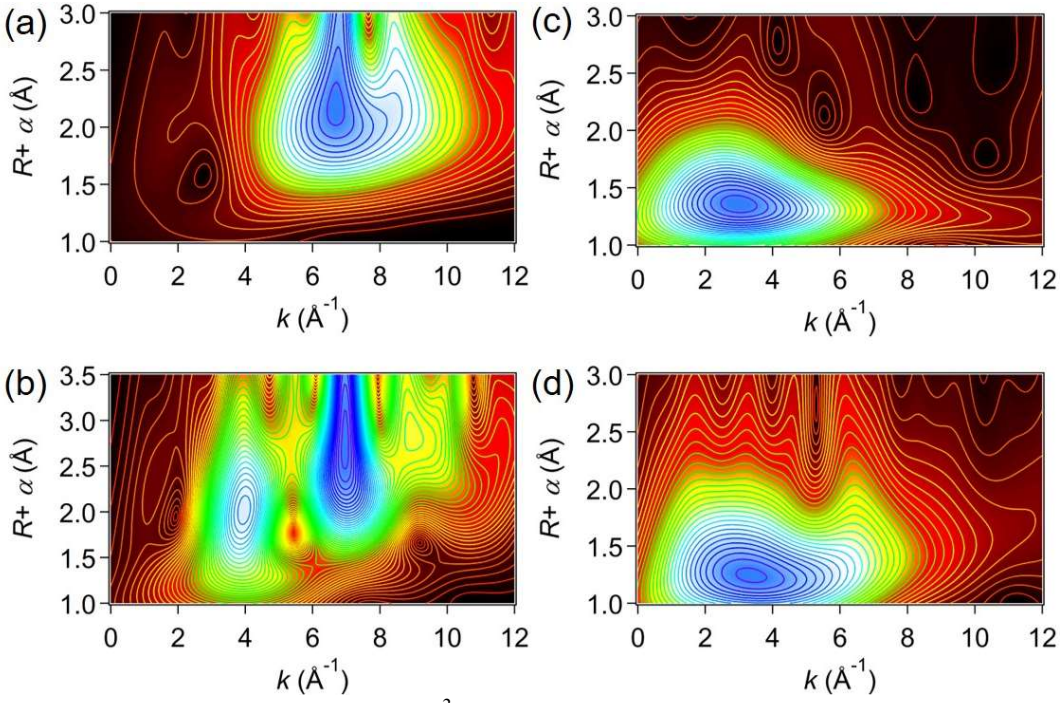

Fig. S21. Wavelet transforms for the k^3-weighted Ni K-edge EXAFS signals of (a) Ni foil, (b) NiO, (c) AD-$Co_{0.48}Ni_{0.52}$, and (d) AD-Co_0Ni_1.

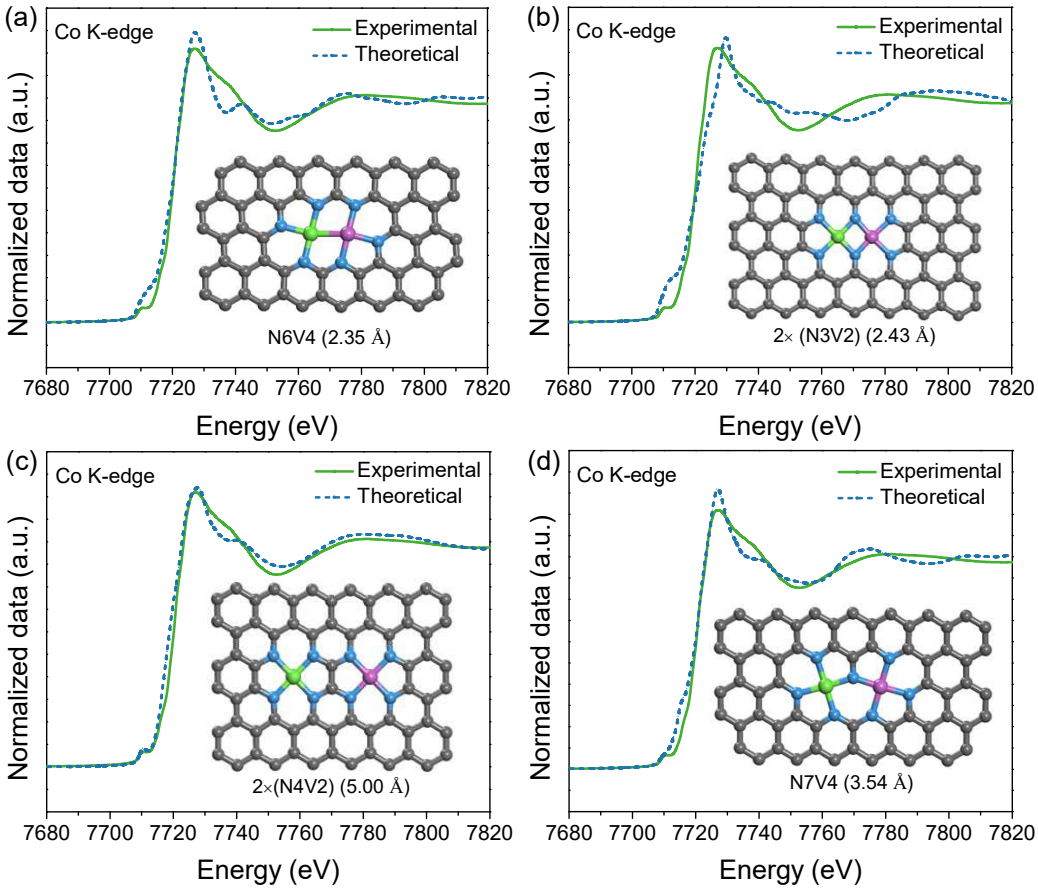

Fig. S22. Theoretical Co K-edge XANES spectra of the proposed models of (a) N6V4-CoNi, (b) 2×(N3V2)-CoNi, (c) 2×(N4V2)-CoNi, and (d) N7V4-CoNi.

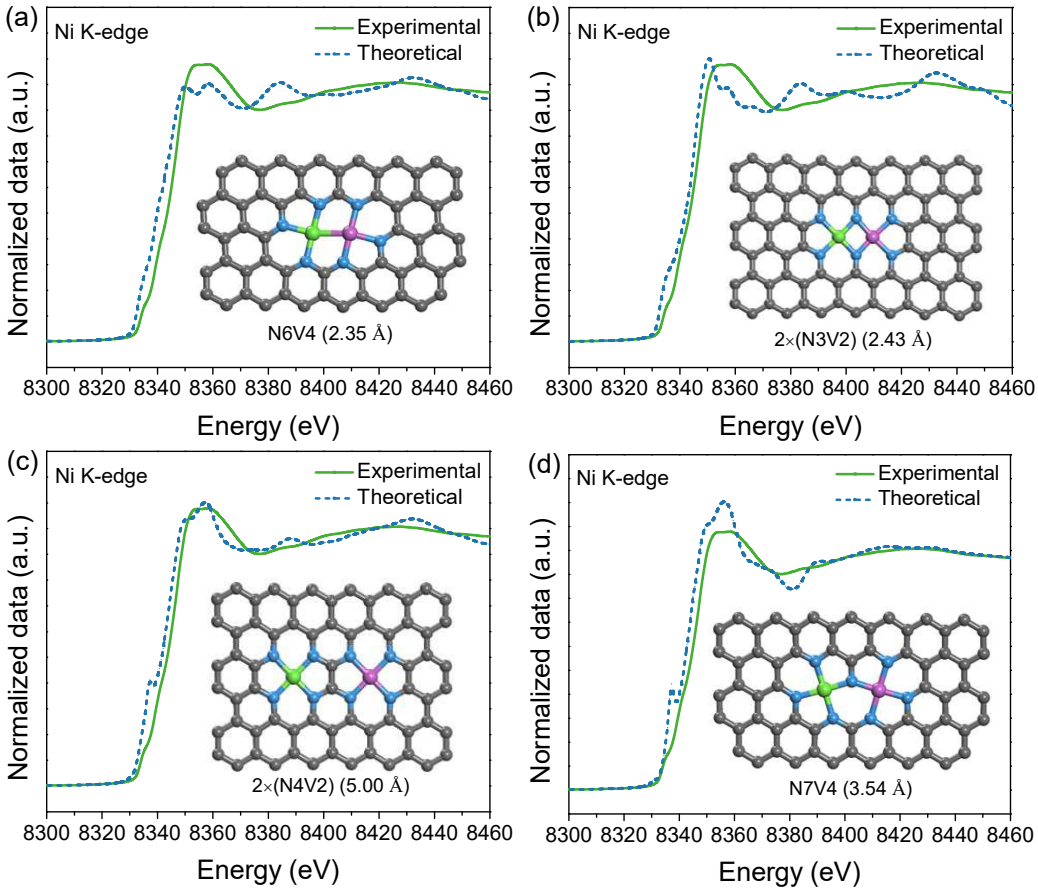

Fig. S23. Theoretical Ni K-edge XANES spectra of the proposed models of (a) N6V4-CoNi, (b) 2×(N3V2)-CoNi, (c) 2×(N4V2)-CoNi, and (d) N7V4-CoNi.

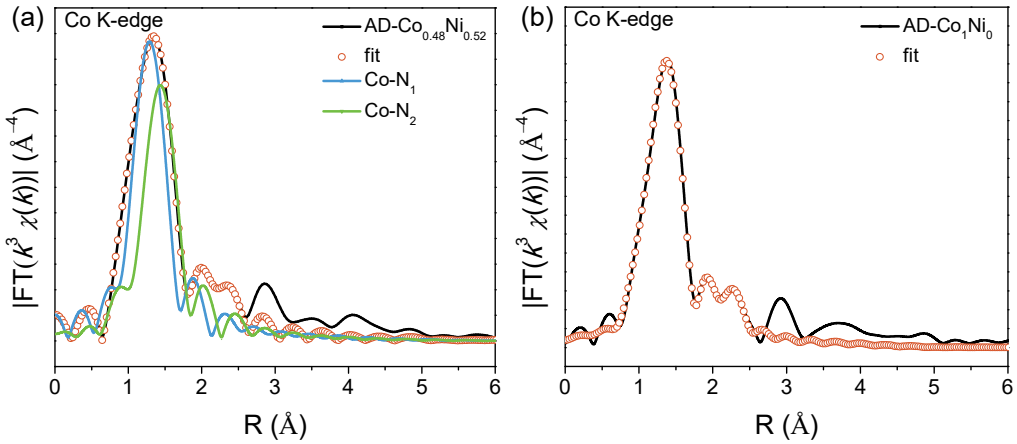

Fig. S24. Co K-edge EXAFS spectra fitting of (a) AD-$Co_{0.48}Ni_{0.52}$ and (b) AD-Co_1Ni_0.

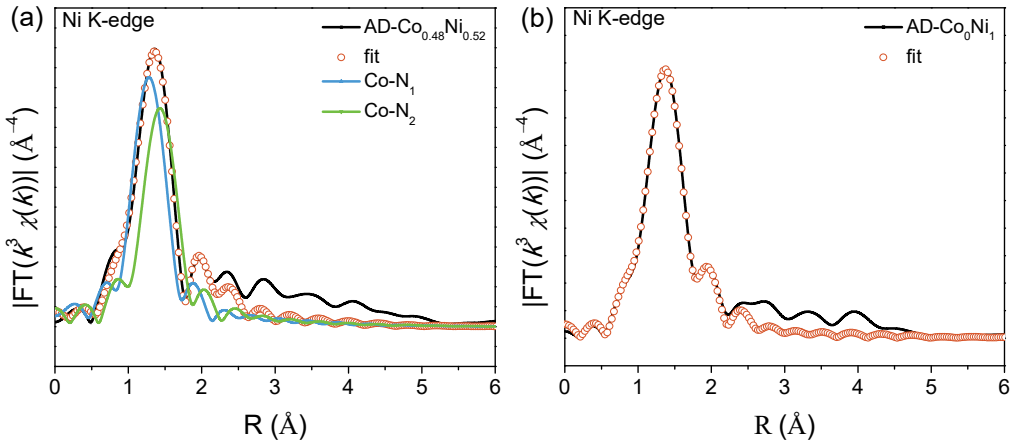

Fig. S25. Ni K-edge EXAFS spectra fitting of (a) AD-$Co_{0.48}Ni_{0.52}$ and (b) AD-Co_0Ni_1.

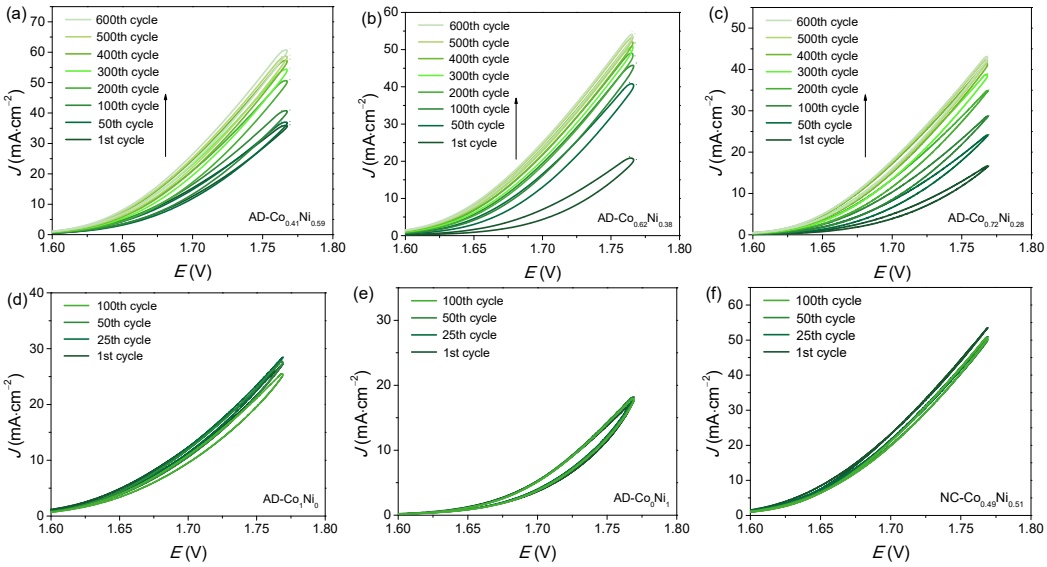

Fig. S26. OER CV curves of (a) AD-$Co_{0.41}Ni_{0.59}$, (b) AD-$Co_{0.62}Ni_{0.38}$, (c) AD-$Co_{0.72}Ni_{0.28}$, (d) AD-Co_1Ni_0, (e) AD-Co_0Ni_1, and (f) NC-$Co_{0.49}Ni_{0.51}$.

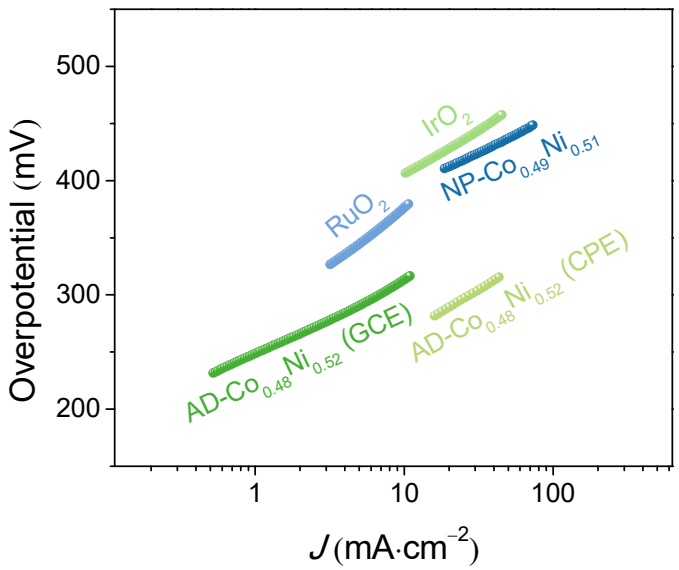

Fig. S27. OER Tafel slopes for AD-$Co_{0.48}Ni_{0.52}$ (GCE), AD-$Co_{0.48}Ni_{0.52}$ (CPE), NC-$Co_{0.49}Ni_{0.51}$, RuO_2, and IrO_2.

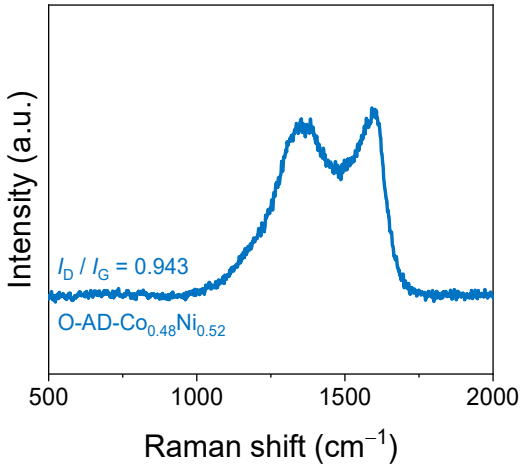

Fig. S28. Raman spectra of AD-$Co_{0.48}Ni_{0.52}$ after OER.

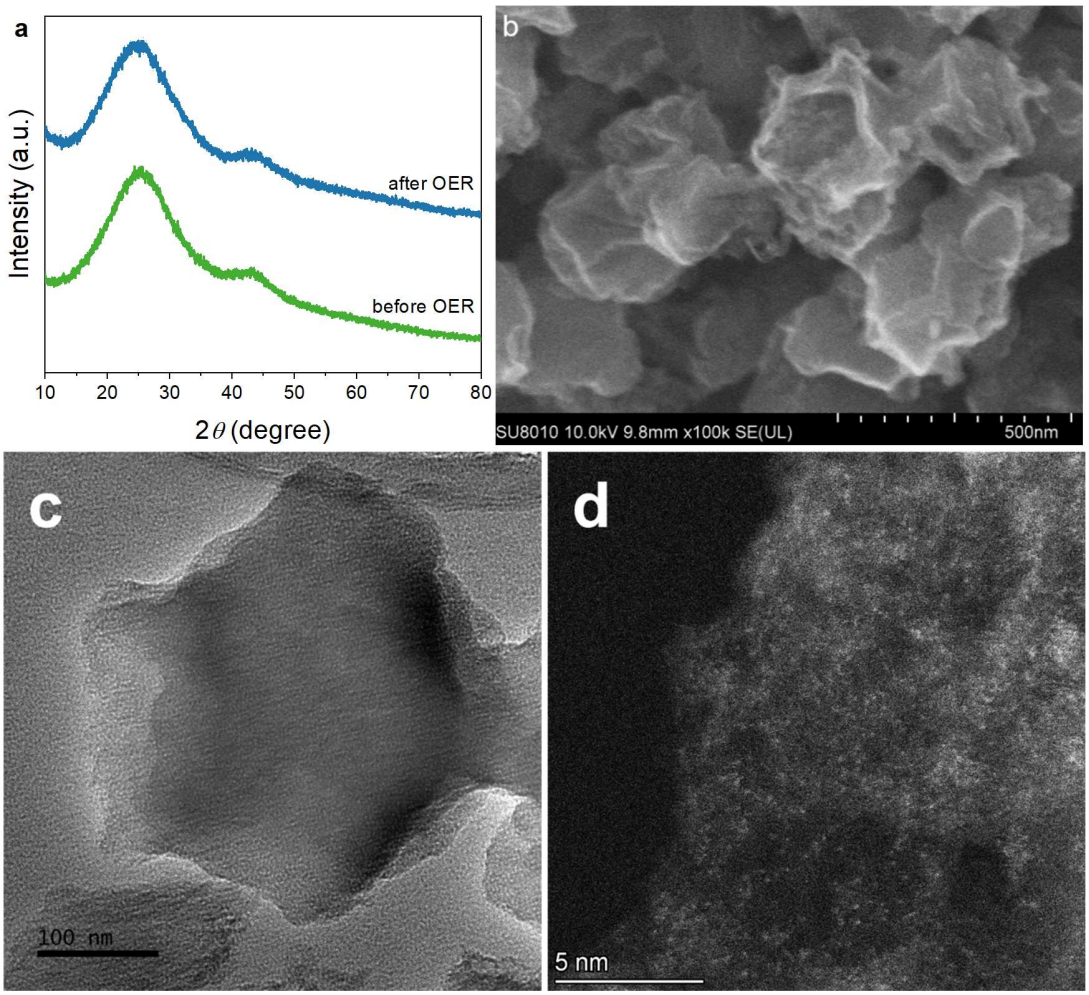

Fig. S29. (a) PXRD patterns of AD-$Co_{0.48}Ni_{0.52}$ before and after OER. (b) SEM, (c)TEM and (d) HADDF-STEM image of AD-$Co_{0.48}Ni_{0.52}$ after OER.

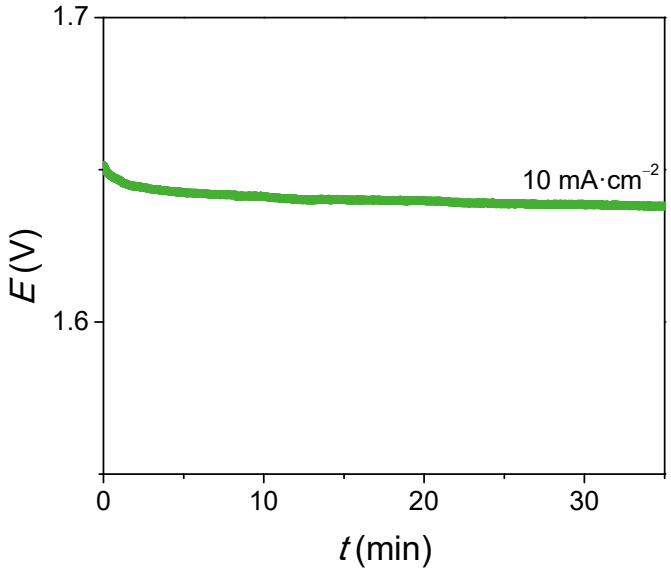

Fig. S30. OER chronopotentiometry curve of AD-$Co_{0.48}Ni_{0.52}$ at 10 mA·cm^{-2} during operando ATR-FTIR (Fig. 4a).

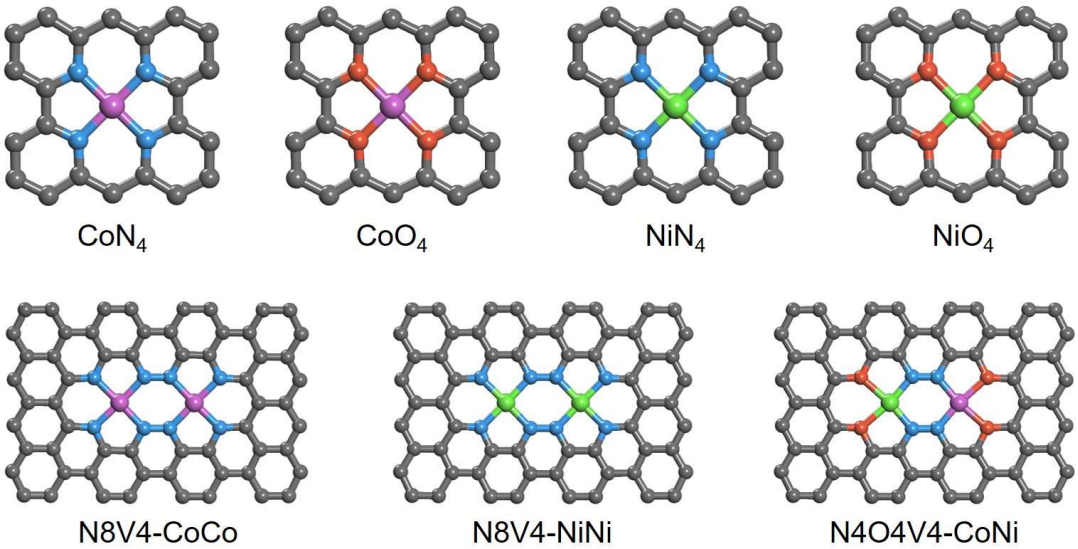

Fig. S31. Structures of the CoN_4, CoO_4, NiN_4, NiO_4, N8V4-CoCo, N8V4-NiNi, and N4O4V4-CoNi models.

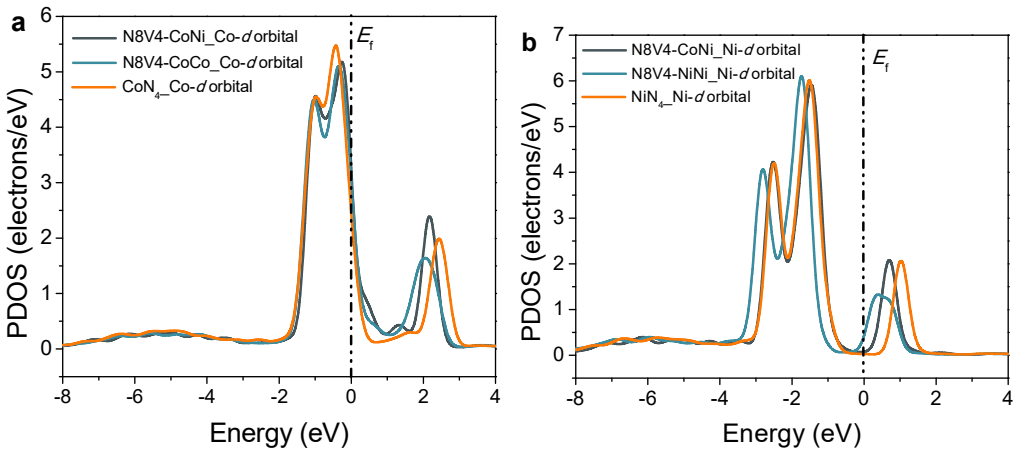

Fig. S32. DFT derived partial DOS of (a) Co-d-orbital in N8V4-CoNi, N8V4-CoCo and CoN_4 and (b) Ni-d-orbital in N8V4-CoNi, N8V4-NiNi and NiN_4.

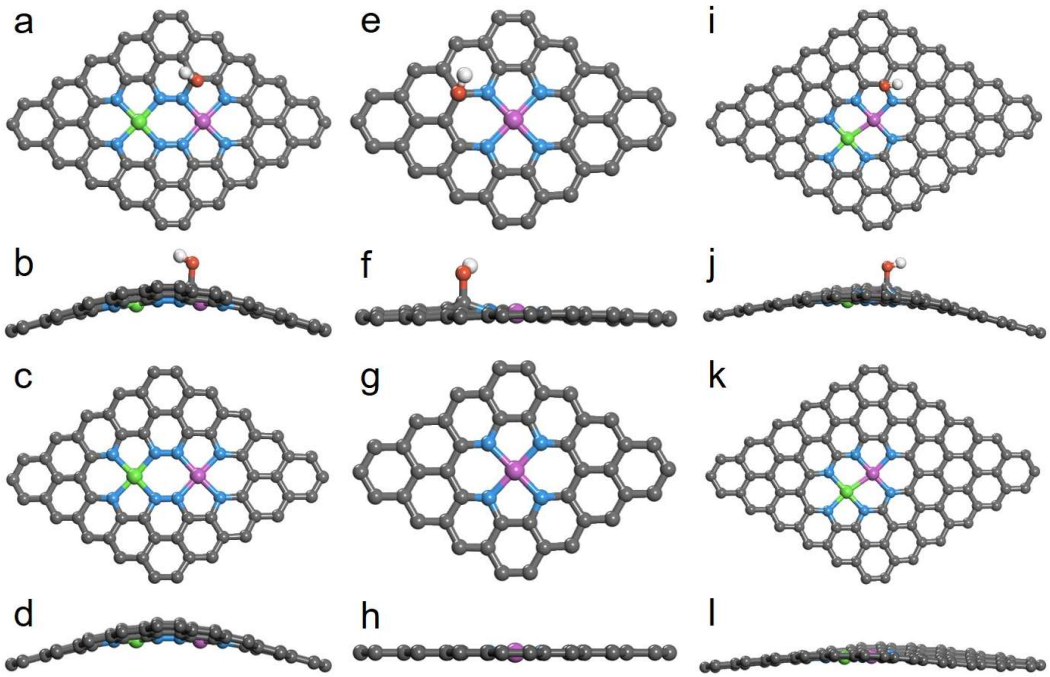

Fig. S33. The graphene matrix inlaid with (a and b) N8V4-CoNi-OH, (c and d) N8V4-CoNi, (e and f) CoN_4-OH, (g and h) CoN_4, (i and j) N6V4-CoNi-OH, and (k and l) N6V4-CoNi.

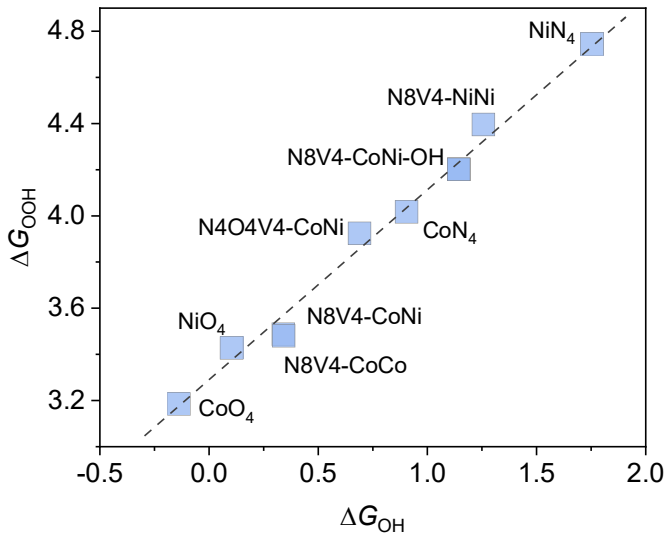

Fig. S34. Scaling relation between the binding energies for OH and OOH.

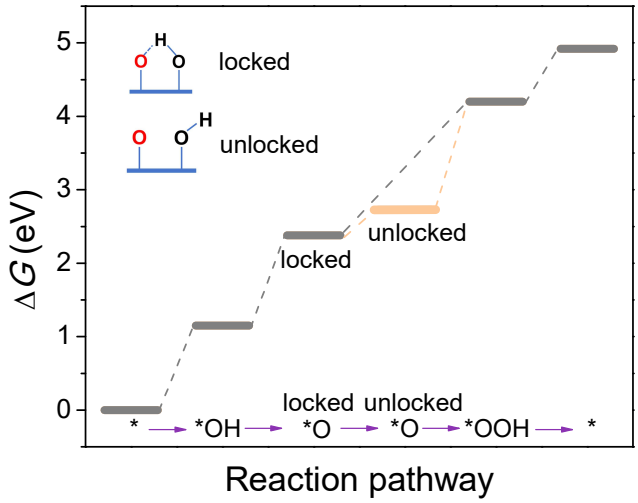

Fig. S35. Scaling relationship of AD-$Co_{0.48}Ni_{0.52}$ for OER.

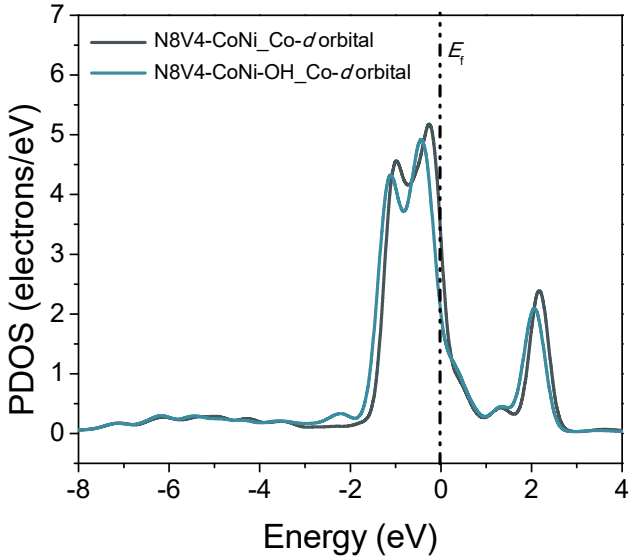

Fig. S36. DFT derived partial DOS of (a) Co-d-orbital in N8V4-CoNi, N8V4-CoNi-OH.

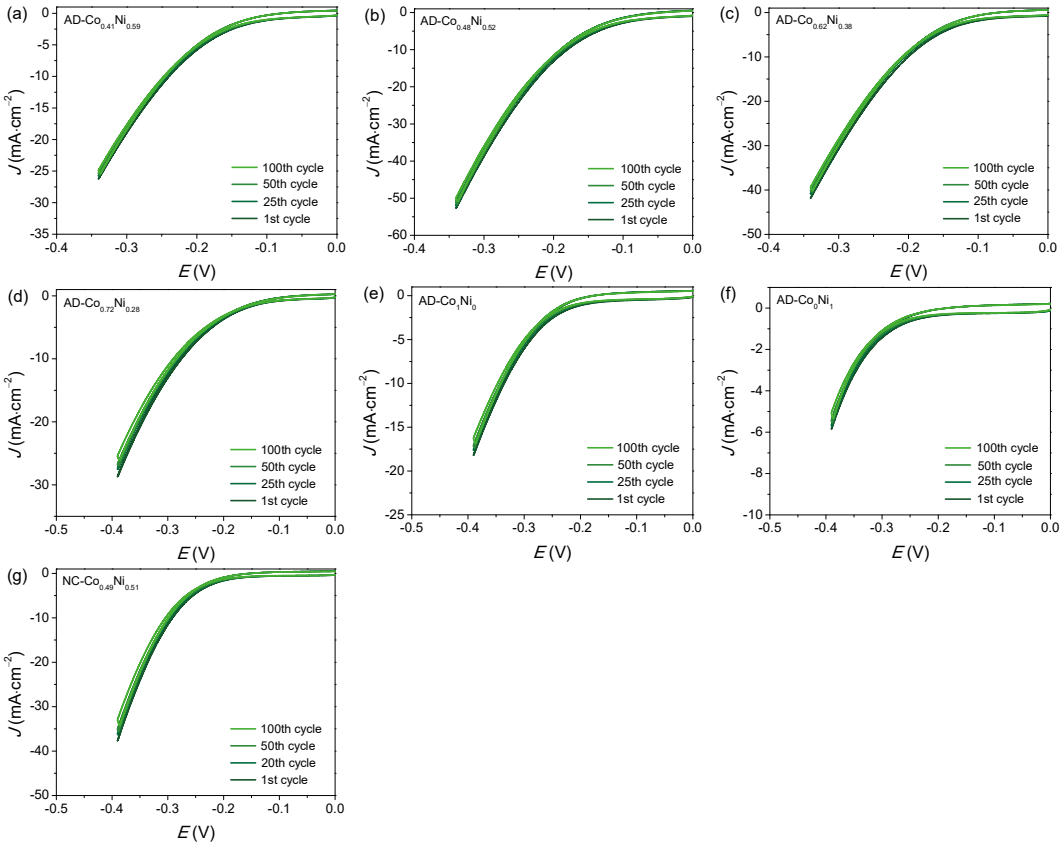

Fig. S37. HER CV curves of (a) AD-$Co_{0.41}Ni_{0.59}$, (b) AD-$Co_{0.48}Ni_{0.52}$, (c) AD-$Co_{0.62}Ni_{0.38}$, (d) AD-$Co_{0.72}Ni_{0.28}$, (e) AD-Co_1Ni_0, (f) AD-Co_0Ni_1, and (g) NC-$Co_{0.49}Ni_{0.51}$.

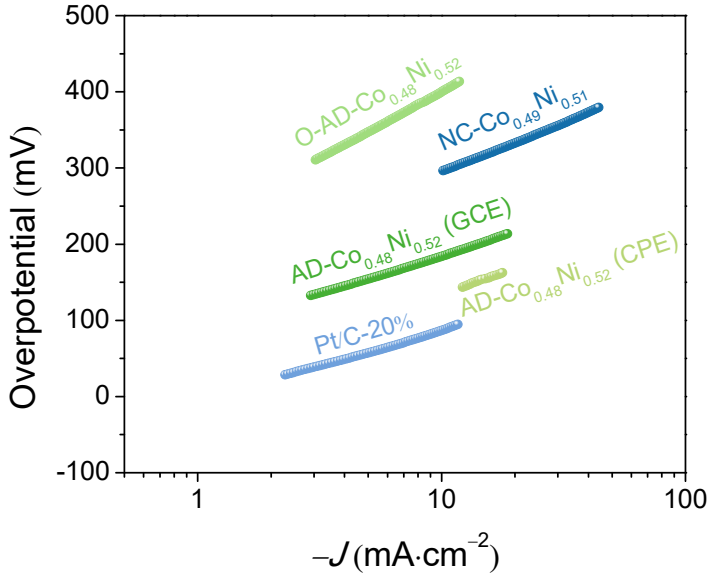

Fig. S38. HER Tafel slopes for AD-$Co_{0.48}Ni_{0.52}$ (GCE), AD-$Co_{0.48}Ni_{0.52}$ (CPE), NC-$Co_{0.49}Ni_{0.51}$, O-AD-$Co_{0.48}Ni_{0.52}$, and Pt/C-20%.

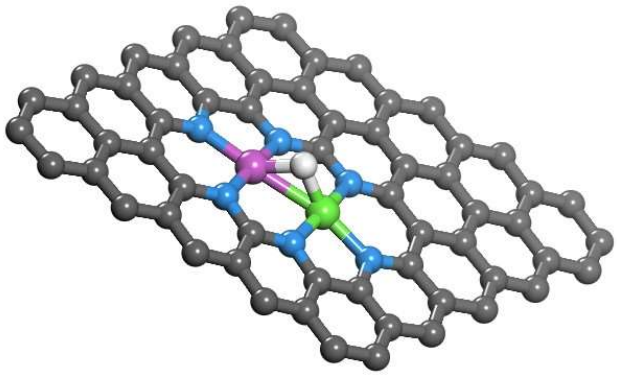

Fig. S39. Hydrogen intermediate adsorbed on the N6V4-CoNi model.

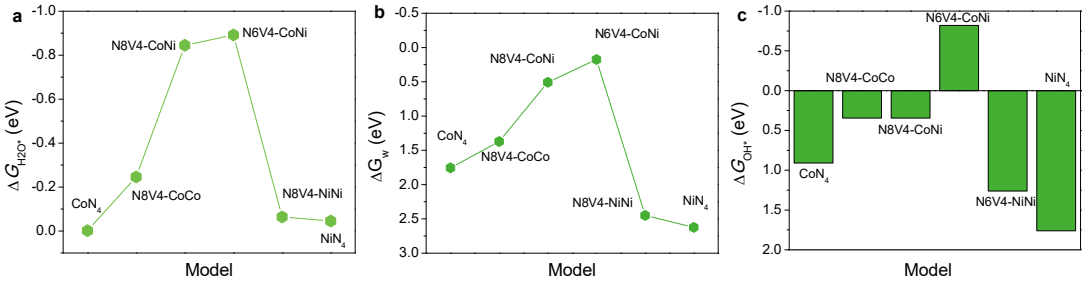

Fig. 40. Scaling relationship of (a) H_2O adsorption energy, (b) H_2O dissociation energy, and (c) OH* adsorption energy in CoN_4, N8V4-CoCo, N8V4-CoNi, N6V4-CoNi, N8V4-NiNi and NiN_4 for HER.

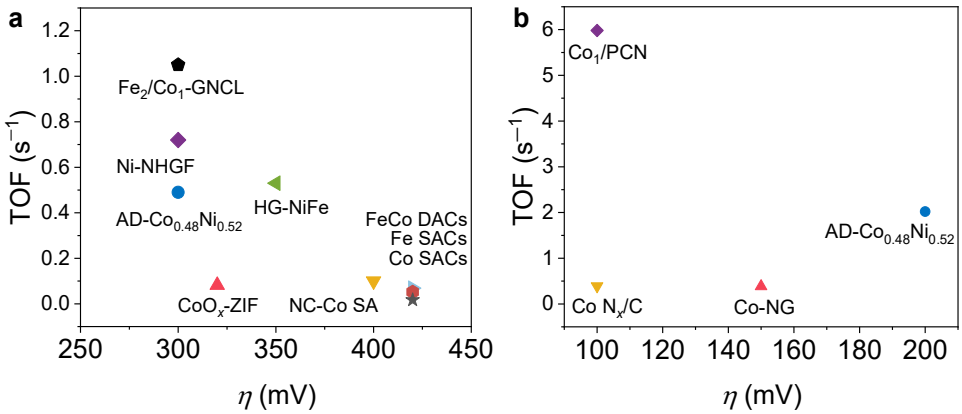

Fig. S41. TOF values of AD-$Co_{0.48}Ni_{0.52}$ and other atomically dispersed electrocatalysts.

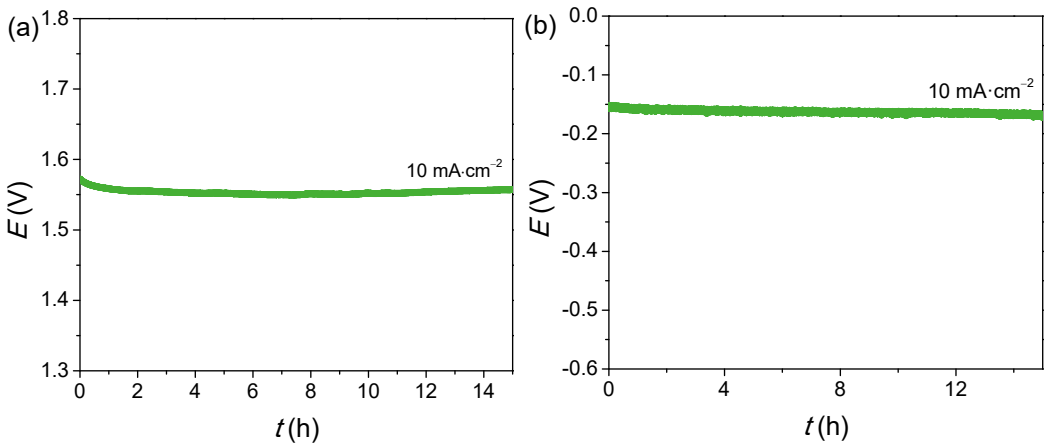

Fig. 42. (a) OER and (b) HER chronopotentiometry curves for AD-$Co_{0.48}Ni_{0.52}$ coated on CPE.

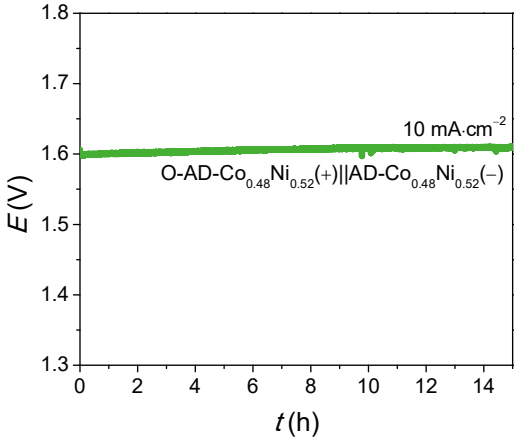

Fig. S43. Chronopotentiometry curve of O-AD-$Co_{0.48}Ni_{0.52}$(+)‖AD-$Co_{0.48}Ni_{0.52}$(−) for overall water splitting.

Table S1. The feeding parameters for Co/Ni-doped MAF-4.

Feeding amounts			Pyrolysis product
z	*c*	*n*	
3.5	0.109	0	AD-Co_1Ni_0
3.5	0.078	0.124	AD-$Co_{0.72}Ni_{0.28}$
3.5	0.068	0.168	AD-$Co_{0.62}Ni_{0.38}$
3.5	0.055	0.238	AD-$Co_{0.48}Ni_{0.52}$
3.5	0.044	0.261	AD-$Co_{0.41}Ni_{0.59}$
3.5	0	0.475	AD-Co_0Ni_1
3.4	0.081	0.358	Not studied because of the uncertain structure of metal species
3.3	0.110	0.479	
3.2	0.175	0.741	NC-$Co_{0.49}Ni_{0.51}$

Table S2. Structural parameters extracted from the Co K-edge and Ni K-edge EXAFS fitting. (S_0^2 = 0.81 for Co K-edge and 0.85 for Ni K-edge)

Sample	Edge	Scattering pair	*N*	*R* (Å)	σ^2 (10^{-3} Å^2)	ΔE_0 (eV)	*R* factor
AD-$Co_{0.48}Ni_{0.52}$	Co	Co-N1	2.2	1.93	5.4	1.0	0.005
		Co-N2	1.9	1.97	5.9		
	Ni	Ni-N1	2.1	1.94	5.1	1.5	0.006
		Ni-N2	2.0	1.99	5.7		
AD-Co_1Ni_0	Co	Co-N	4.1	1.95	4.6	1.5	0.007
AD-Co_0Ni_1	Ni	Ni-N	3.9	1.96	4.9	1.5	0.004

S_0^2 is the amplitude reduction factor; *N* is the coordination number; *R* is interatomic distance (the bond length between Co/Ni central atoms and surrounding coordination atoms); σ^2 is the Debye-Waller factor value (a measure of thermal and static disorder in absorber-scatterer distances); ΔE_0 is edge-energy shift (the difference between the zero kinetic energy value of the sample and that of the theoretical model); *R* factor is used to value the goodness of the fitting.

Error bounds that characterize the structural parameters obtained by EXAFS spectroscopy were estimated as $N \pm 20\%$; $R \pm 1\%$; $\sigma^2 \pm 20\%$; $\Delta E_0 \pm 20\%$.

Table S3. Determination of the F:O atomic ratio of AD-$Co_{0.48}Ni_{0.52}$ before and after OER.

	F	O	F:O
Before OER	41.35	5.66	7.31:1
After OER	36.78	6.96	5.28:1

Fluorine (F) was from Nafion.

Table S4. The energy change after oxidation to form C-OH.

Model	before oxidation	*E* (eV)	after oxidation	*E* (eV)	Δ*E* (eV)
N8V4-CoNi	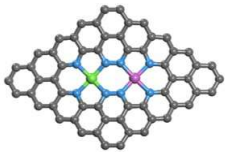	−14149.6	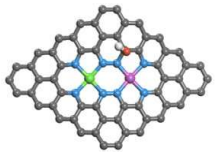	−14604.6	1.08
CoN_4	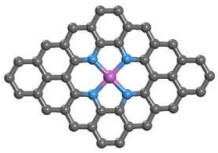	−12647.9	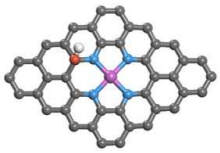	−13102.9	1.63
N6V4-CoNi	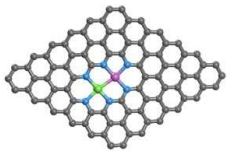	−20348.6	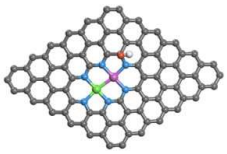	−20803.9	1.48

Table S5. The calculated energy of the oxidation position on N8V4-CoNi.

before oxidation	*E* (eV)	after oxidation	*E* (eV)	Δ*E* (eV)
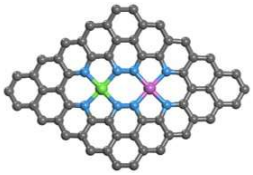	−14149.6	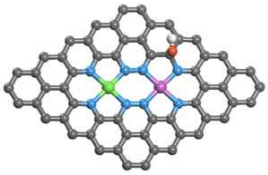	−14604.2	1.512
		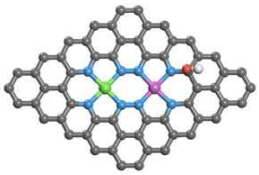	−14603.8	1.860
		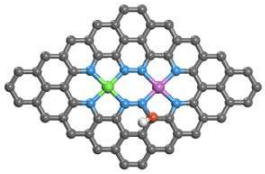	−14604.0	1.658
		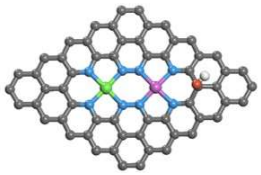	−14604.0	1.692
		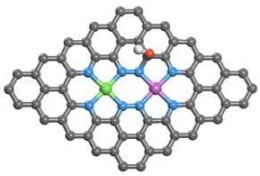	−14604.6	1.080

Table S6. Benchmark electrocatalytic performances of ADCs.

Catalysts	Electrolyte	$\eta_{10\text{-OER}}$ / mV	$\eta_{10\text{-HER}}$ / mV	Substrate	Refs.
AD-$Co_{0.48}Ni_{0.52}$	1.0 M KOH	313	183	GCE	this work
		264	132	CPE	
A-Ni@DG	1 M KOH	270	150	GCE	[2]
DG		340	N.A.		
Fe-N_4 SAs/NPC	1.0 M KOH	430	202	GCE	[3]
CoSA/N,S-HCS	1 M KOH	306	165	CPE	[4]
Ru/Co-N-C	1 M KOH	276	19	CPE	[5]
FeCo-DACs/NC	1.0 M	370	N.A.	CPE	[6]
NiFe-CNG	1 M KOH	270	N.A.	GCE	[7]
NiFe-DASC	1 M KOH	310	N.A.	GCE	[8]
Co-Fe-N-C	1 M KOH	360	N.A.	GCE	[9]
		321	N.A.	CC	
Fe_2/Co_1-GNCL	1 M KOH	350	N.A.	GCE	[10]
Fe_2-GNCL		355	N.A.		
NiFe@g-C_3N_4/CNT	1 M KOH	326	N.A.	GCE	[11]
FeNi@PCN	1 M KOH	310	N.A.	GCE	[12]
CoNi-SAs/NC	1 M KOH	340	N.A.	CC	[13]
a-NiCo/NC	1.0 M KOH	252	N.A.	CC	[14]
Co-C_3N_4/CNT	1 M KOH	380	N.A.	GCE	[15]
Co SA@NCF/CNF	1 M KOH	400	N.A.	CC	[16]
Ni-O-G SACs	1 M KOH	328	N.A.	CC	[17]
0.7-Co@NG-750	1.0 M KOH	386	N.A.	GCE	[18]
Ni-NHGF	1 M KOH	331	N.A.	GCE	[19]
Co-NHGF		402	N.A.		
Fe-NHGF		488	N.A.		
NHGF		494	N.A.		
Mn-NG	1.0 M KOH	337	N.A.	GCE	[20]
Mn-G		459	N.A.		
NC-Co SA	1 M KOH	360	N.A.	CC	[21]
Ni-O-G SACs	1 M KOH	224	N.A.	CC	[22]
Co-NG-5010-10	1 M KOH	470	N.A.	GCE	[23]
Ni-CN-200	1.0 M KOH	310 (onset)	N.A.	GCE	[24]
S,N-Fe/N/C-CNT	0.1 M KOH	370	N.A.	GCE	[25]
CoN_4/NG	0.1 M KOH	380	N.A.	GCE	[26]
Ni-N_4/GHSs/Fe-N_4	0.1 M KOH	390	N.A.	GCE	[27]
(Fe,Co)-SA/CS	0.1 M KOH	360	N.A.	Ni foam	[28]
Co-NG	1 M KOH	N.A.	270	GCE	[29]
CoN_x/G	1.0 M KOH	N.A.	170	GCE	[30]
Co_1/PCN	1.0 M KOH	N.A.	89	Ni foam	[31]
Co_1/CN		N.A.	138		

Table S7. Benchmark performances of bifunctional electrocatalysts for overall water splitting in 1 M KOH. (Blue: ADCs, green: quasi-bifunctional electrocatalysts, red: other bifunctional electrocatalysts)

Catalysts	Substrate	Cell voltages-η_{10} / V	Refs.
O-AD-$Co_{0.48}Ni_{0.52}$(+)‖AD-$Co_{0.48}Ni_{0.52}$(−)	CPE	1.60	this work
Fe-N_4 SAs/NPC	CPE	1.67	[3]
CoSA/N,S-HCS	CPE	1.64	[4]
Ru/Co-N-C	CPE	1.50	[5]
Fe-O_2cat(+)‖Fe-H_2cat(−)	Fe foam	1.65	[32]
R-CoO_x@CN(+)‖R-CoO_x@CN(−)	Ni foam	1.6	[33]
Ni_2P/NiO_x (+)‖Ni_2P(−)	Ni foam	1.63	[34]
Ir_1@Co/NC	CPE	1.60	[35]
CoP/NCNHP	CPE	1.64	[36]
CoP/rGO	CPE	1.7	[37]
Co-S sheets	CPE	1.743	[38]
Co_3O_4 NCs	CPE	1.91	[39]
Co-P/NC	GCE	1.71	[40]
Co_1Mn_1CH	Ni foam	1.68	[41]
NiFe LDH	Ni foam	1.7	[42]
$NiCo_2O_4$	Ni foam	1.65	[43]
$Co_{0.85}$Se/NiFe-LDH	graphite foil	1.67	[44]
Ni_3S_2	Ni foam	1.76	[45]
Cu@CoS_x	Cu foam	1.5	[46]
Cu@NiFe LDH	Cu foam	1.54	[47]

References

1. B. Ravel, M. Newville, ATHENA, ARTEMIS, HEPHAESTUS: data analysis for X-ray absorption spectroscopy using IFEFFIT. J. Synchrotron Radiat. **12**, 537-541 (2005). https://doi.org/10.1107/S0909049505012719
2. L. Zhang, Y. Jia, G. Gao, X. Yan, N. Chen, et al., Graphene defects trap atomic Ni species for hydrogen and oxygen evolution reactions. Chem **4**, 285-297 (2018). https://doi.org/10.1016/j.chempr.2017.12.005
3. Y. Pan, S. Liu, K. Sun, X. Chen, B. Wang, et al., A bimetallic Zn/Fe polyphthalocyanine-derived single-atom Fe-N_4 catalytic site: a superior trifunctional catalyst for overall water splitting and Zn-air batteries. Angew. Chem. Int. Ed. **57**, 8614-8618 (2018). https://doi.org/10.1002/anie.201804349
4. Z. Zhang, X. Zhao, S. Xi, L. Zhang, Z. Chen, et al., Atomically dispersed cobalt trifunctional electrocatalysts with tailored coordination environment for flexible rechargeable Zn-air battery and self-driven water splitting. Adv. Energy Mater. **10**, 2002896 (2020). https://doi.org/10.1002/aenm.202002896
5. C. Rong, X. Shen, Y. Wang, L. Thomsen, T. Zhao, et al., Electronic structure engineering of single-atom Ru sites via Co-N_4 sites for bifunctional pH-universal water splitting. Adv. Mater. **34**, 2110103 (2022). https://doi.org/10.1002/adma.202110103
6. M. Liu, N. Li, S. Cao, X. Wang, X. Lu, et al., A "pre-constrained metal twins" strategy to prepare efficient dual-metal-atom catalysts for cooperative oxygen electrocatalysis. Adv. Mater. **34**, 2107421 (2022). https://doi.org/10.1002/adma.202107421
7. W. Wan, Y. Zhao, S. Wei, C.A. Triana, J. Li, et al., Mechanistic insight into the active centers of single/dual-atom Ni/Fe-based oxygen electrocatalysts. Nat. Commun. **12**, 5589 (2021). https://doi.org/10.1038/s41467-021-25811-0
8. Z. Zeng, L.Y. Gan, H. Bin Yang, X. Su, J. Gao, et al., Orbital coupling of hetero-diatomic nickel-iron site for bifunctional electrocatalysis of CO_2 reduction and oxygen evolution. Nat. Commun. **12**, 4088 (2021). https://doi.org/10.1038/s41467-021-24052-5
9. L. Bai, C.S. Hsu, D.T.L. Alexander, H.M. Chen, X. Hu, A cobalt-iron double-atom catalyst for the oxygen evolution reaction. J. Am. Chem. Soc. **141**, 14190-14199 (2019). https://doi.org/10.1021/jacs.9b05268
10. Y.-S. Wei, L. Sun, M. Wang, J. Hong, L. Zou, et al., Fabricating dual-atom iron catalysts for efficient oxygen evolution reaction: a heteroatom modulator approach. Angew. Chem. Int. Ed. **59**, 16013-16022 (2020). https://doi.org/10.1002/anie.202007221
11. D. Liu, S. Ding, C. Wu, W. Gan, C. Wang, et al., Synergistic effect of an atomically dual-metal doped catalyst for highly efficient oxygen evolution. J. Mater. Chem. A **6**, 6840-6846 (2018). https://doi.org/10.1039/c8ta00550h
12. C. Wu, X. Zhang, Z. Xia, M. Shu, H. Li, et al., Insight into the role of Ni-Fe dual sites in the oxygen evolution reaction based on atomically metal-doped polymeric carbon nitride. J. Mater. Chem. A **7**, 14001-14010 (2019). https://doi.org/10.1039/c9ta03163d
13. X. Han, X. Ling, D. Yu, D. Xie, L. Li, et al., Atomically dispersed binary Co-Ni sites in nitrogen-doped hollow carbon nanocubes for reversible oxygen reduction and evolution. Adv. Mater. **31**, 1905622 (2019). https://doi.org/10.1002/adma.201905622
14. Z. Pei, X.F. Lu, H. Zhang, Y. Li, D. Luan, et al., Highly efficient electrocatalytic oxygen evolution over atomically dispersed synergistic Ni/Co dual sites. Angew. Chem. Int. Ed. **61**, 202207537 (2022) https://doi.org/10.1002/anie.202207537.
15. Y. Zheng, Y. Jiao, Y. Zhu, Q. Cai, A. Vasileff, et al., Molecule-level g-C_3N_4 coordinated transition metals as a new class of electrocatalysts for oxygen electrode reactions. J. Am. Chem. Soc. **139**, 3336-3339 (2017). https://doi.org/10.1021/jacs.6b13100
16. D. Ji, L. Fan, L. Li, S. Peng, D. Yu, et al., Atomically transition metals on self-supported porous carbon flake arrays as binder-free air cathode for wearable zinc-air batteries. Adv. Mater. **31**, 1808267 (2019). https://doi.org/10.1002/adma.201808267
17. Y. Xu, W. Zhang, Y. Li, P. Lu, Z.-S. Wu, A general bimetal-ion adsorption strategy to prepare nickel single atom catalysts anchored on graphene for efficient oxygen evolution reaction. J. Energy Chem. **43**, 52-57 (2020). https://doi.org/10.1016/j.jechem.2019.08.006
18. Q. Zhang, Z. Duan, M. Li, J. Guan, Atomic cobalt catalysts for the oxygen evolution reaction. Chem. Commun. **56**, 794-797 (2020). https://doi.org/10.1039/c9cc09007j
19. H. Fei, J. Dong, Y. Feng, C.S. Allen, C. Wan, et al., General synthesis and definitive structural identification of MN_4C4 single-atom catalysts with tunable electrocatalytic activities. Nat. Catal. **1**, 63-72 (2018). https://doi.org/10.1038/s41929-017-0008-y
20. J. Guan, Z. Duan, F. Zhang, S.D. Kelly, R. Si, et al., Water oxidation on a mononuclear manganese

heterogeneous catalyst. Nat. Catal. **1**, 870-877 (2018). https://doi.org/10.1038/s41929-018-0158-6
21. W. Zang, A. Sumboja, Y. Ma, H. Zhang, Y. Wu, et al., Single Co atoms anchored in porous N-doped carbon for efficient zinc-air battery cathodes. ACS Catal. **8**, 8961-8969 (2018). https://doi.org/10.1021/acscatal.8b02556
22. Y. Li, Z.S. Wu, P. Lu, X. Wang, W. Liu, et al., High-valence nickel single-atom catalysts coordinated to oxygen sites for extraordinarily activating oxygen evolution reaction. Adv. Sci. **7**, 1903089 (2020). https://doi.org/10.1002/advs.201903089
23. Y. Zhang, W. Li, L. Lu, W. Song, C. Wang, et al., Tuning active sites on cobalt/nitrogen doped graphene for electrocatalytic hydrogen and oxygen evolution. Electrochim. Acta. **265**, 497-506 (2018). https://doi.org/10.1016/j.electacta.2018.01.203
24. S. Ohn, S.Y. Kim, S.K. Mun, J. Oh, Y.J. Sa, et al., Molecularly dispersed nickel-containing species on the carbon nitride network as electrocatalysts for the oxygen evolution reaction. Carbon **124**, 180-187 (2017). https://doi.org/10.1016/j.carbon.2017.08.039
25. P. Chen, T. Zhou, L. Xing, K. Xu, Y. Tong, et al., Atomically dispersed iron-nitrogen species as electrocatalysts for bifunctional oxygen evolution and reduction reactions. Angew. Chem. Int. Ed. **56**, 610-614 (2017). https://doi.org/10.1002/anie.201610119
26. L. Yang, L. Shi, D. Wang, Y. Lv, D. Cao, Single-atom cobalt electrocatalysts for foldable solid-state Zn-air battery. Nano Energy **50**, 691-698 (2018). https://doi.org/10.1016/j.nanoen.2018.06.023
27. J. Chen, H. Li, C. Fan, Q. Meng, Y. Tang, et al., Dual single-atomic Ni-N_4 and Fe-N_4 sites constructing Janus hollow graphene for welective oxygen electrocatalysis. Adv. Mater. **32**, 2003134 (2020). https://doi.org/10.1002/adma.202003134
28. V. Jose, H. Hu, E. Edison, W. Manalastas, Jr., H. Ren, et al., Modulation of single atomic Co and Fe sites on hollow carbon nanospheres as oxygen electrodes for rechargeable Zn-air batteries. Small Methods **5**, 2000751 (2021). https://doi.org/10.1002/smtd.202000751
29. H. Fei, J. Dong, M.J. Arellano-Jimenez, G. Ye, N. Dong Kim, et al., Atomic cobalt on nitrogen-doped graphene for hydrogen generation. Nat. Commun. **6**, 8668 (2015). https://doi.org/10.1038/ncomms9668
30. H.W. Liang, S. Bruller, R. Dong, J. Zhang, X. Feng, et al., Molecular metal-N_x centres in porous carbon for electrocatalytic hydrogen evolution. Nat. Commun. **6**, 7992 (2015). https://doi.org/10.1038/ncomms8992
31. L. Cao, Q. Luo, W. Liu, Y. Lin, X. Liu, et al., Identification of single-atom active sites in carbon-based cobalt catalysts during electrocatalytic hydrogen evolution. Nat. Catal. **2**, 134-141 (2018). https://doi.org/10.1038/s41929-018-0203-5
32. X. Zou, Y. Wu, Y. Liu, D. Liu, W. Li, et al., In situ generation of bifunctional, efficient Fe-based catalysts from mackinawite iron sulfide for water splitting. Chem **4**, 1139-1152 (2018). https://doi.org/10.1016/j.chempr.2018.02.023
33. H. Jin, J. Wang, D. Su, Z. Wei, Z. Pang, et al., In situ cobalt-cobalt oxide/N-doped carbon hybrids as superior bifunctional electrocatalysts for hydrogen and oxygen evolution. J. Am. Chem. Soc. **137**, 2688-2694 (2015). https://doi.org/10.1021/ja5127165
34. L.-A. Stern, L. Feng, F. Song, X. Hu, Ni_2P as a Janus catalyst for water splitting: the oxygen evolution activity of Ni2P nanoparticles. Energy Environ. Sci. **8**, 2347-2351 (2015). https://doi.org/10.1039/c5ee01155h
35. W.H. Lai, L.F. Zhang, W.B. Hua, S. Indris, Z.C. Yan, et al., General π-electron-assisted strategy for Ir, Pt, Ru, Pd, Fe, Ni single-atom electrocatalysts with bifunctional active sites for highly efficient water splitting. Angew. Chem. Int. Ed. **58**, 11868-11873 (2019). https://doi.org/10.1002/anie.201904614
36. Y. Pan, K. Sun, S. Liu, X. Cao, K. Wu, et al., Core-shell ZIF-8@ZIF-67-derived CoP nanoparticle-embedded N-doped carbon nanotube hollow polyhedron for efficient overall water splitting. J. Am. Chem. Soc. **140**, 2610-2618 (2018). https://doi.org/10.1021/jacs.7b12420
37. L. Jiao, Y.X. Zhou, H.L. Jiang, Metal-organic framework-based CoP/reduced graphene oxide: high-performance bifunctional electrocatalyst for overall water splitting. Chem. Sci. **7**, 1690-1695 (2016). https://doi.org/10.1039/c5sc04425a
38. J. Wang, H.X. Zhong, Z.L. Wang, F.L. Meng, X.B. Zhang, Integrated three-dimensional carbon paper/carbon tubes/cobalt-sulfide sheets as an efficient electrode for overall water splitting. ACS Nano **10**, 2342-2348 (2016). https://doi.org/10.1021/acsnano.5b07126
39. S. Du, Z. Ren, J. Zhang, J. Wu, W. Xi, et al., Co_3O_4 nanocrystal ink printed on carbon fiber paper as a large-area electrode for electrochemical water splitting. Chem. Commun. **51**, 8066-8069 (2015). https://doi.org/10.1039/c5cc01080b

40. B. You, N. Jiang, M. Sheng, S. Gul, J. Yano, et al., High-performance overall water splitting electrocatalysts derived from cobalt-based metal-organic frameworks. Chem. Mater. **27**, 7636-7642 (2015). https://doi.org/10.1021/acs.chemmater.5b02877
41. T. Tang, W.J. Jiang, S. Niu, N. Liu, H. Luo, et al., Electronic and morphological dual modulation of cobalt carbonate hydroxides by Mn doping toward highly efficient and stable bifunctional electrocatalysts for overall water splitting. J. Am. Chem. Soc. **139**, 8320-8328 (2017). https://doi.org/10.1021/jacs.7b03507
42. J. Luo, J.-H. Im, M.T. Mayer, M. Schreier, M.K. Nazeeruddin, et al., Water photolysis at 12.3% efficiency via perovskite photovoltaics and earth-abundant catalysts. Science **345**, 1593-1596 (2014). https://doi.org/10.1126/science.1258307
43. X. Gao, H. Zhang, Q. Li, X. Yu, Z. Hong, et al., Hierarchical $NiCo_2O_4$ hollow microcuboids as bifunctional electrocatalysts for overall water-splitting. Angew. Chem. Int. Ed. **55**, 6290-6294 (2016). https://doi.org/10.1002/anie.201600525
44. Y. Hou, M.R. Lohe, J. Zhang, S. Liu, X. Zhuang, et al., Vertically oriented cobalt selenide/NiFe layered-double-hydroxide nanosheets supported on exfoliated graphene foil: an efficient 3D electrode for overall water splitting. Energy Environ. Sci. **9**, 478-483 (2016). https://doi.org/10.1039/c5ee03440j
45. L.L. Feng, G. Yu, Y. Wu, G.D. Li, H. Li, et al., High-index faceted Ni_3S_2 nanosheet arrays as highly active and ultrastable electrocatalysts for water splitting. J. Am. Chem. Soc. **137**, 14023-14026 (2015). https://doi.org/10.1021/jacs.5b08186
46. Y. Liu, Q. Li, R. Si, G.D. Li, W. Li, et al., Coupling sub-nanometric copper clusters with quasi-amorphous cobalt sulfide yields efficient and robust electrocatalysts for water splitting reaction. Adv. Mater. **29**, 1606200 (2017). https://doi.org/10.1002/adma.201606200
47. L. Yu, H. Zhou, J. Sun, F. Qin, F. Yu, et al., Cu nanowires shelled with NiFe layered double hydroxide nanosheets as bifunctional electrocatalysts for overall water splitting. Energy Environ. Sci. **10**, 1820-1827 (2017). https://doi.org/10.1039/c7ee01571b